Collectivity of the $2p - 2h$ proton intruder band of ^{116}Sn

C. M. Petrache,[1, *] J.-M. Régis,[2] C. Andreoiu,[3] M. Spieker,[4] C. Michelagnoli,[5] P. E. Garrett,[6] A. Astier,[1] E. Dupont,[1] F. Garcia,[3] S. Guo,[7] G. Häfner,[2] J. Jolie,[2] F. Kandzia,[5] V. Karayonchev,[2] Y.-H. Kim,[5] L. Knafla,[2] U. Köster,[5] B. F. Lv,[1, 7] N. Marginean,[8] C. Mihai,[8] P. Mutti,[5] K. Ortner,[3] C. Porzio,[5, 9] S. Prill,[2] N. Saed-Samii,[2] W. Urban,[10] J. R. Vanhoy,[11] K. Whitmore,[3] J. Wisniewski,[10] and S. W. Yates[12]

[1]*Centre de Sciences Nucléaires et Sciences de la Matière, CNRS/IN2P3,*
Université Paris-Saclay, Bât. 104-108, 91405 Orsay, France
[2]*Institut für Kernphysik, Universität zu Köln, Zülpicher Str. 77, 50937 Köln, Germany*
[3]*Department of Chemistry, Simon Fraser University, Burnaby, BC V5A 1S6, Canada*
[4]*National Superconducting Cyclotron Laboratory, Michigan State University,*
640 South Shaw Lane, East Lansing, MI 48824, USA
[5]*Institut Laue-Langevin, 71 Avenue des Martyrs, F-38042 Grenoble, France*
[6]*Department of Physics, University of Guelph, Guelph, Ontario N1G 2W1, Canada NIG*
[7]*Institute of Modern Physics, Chinese Academy of Sciences, Lanzhou 730000, China*
[8]*Horia Hulubei National Institute for Physics and Nuclear Engineering, 77125 Bucharest, Romania*
[9]*INFN Sez. of Milano and Dipartimento di Fisica, Università di Milano, Milano, Italy*
[10]*Faculty of Physics, University of Warsaw, ulica Pasteura 5, PL-02-093 Warsaw, Poland*
[11]*Physics Department, United States Naval Academy, Annapolis, MD 21402, USA*
[12]*University of Kentucky, Lexington, KY 40506-0055 USA*
(Dated:)

The half-life of the 4_2^+ state of the $2p - 2h$ proton intruder band of ^{116}Sn has been measured for the first time with the fast-timing technique. The lifetime of $T_{1/2} = 29(10)$ ps leads to a transition probability $B(E2; 4_2^+ \to 2_2^+) = 40(13)$ Weisskopf units, which is in very good agreement with the large $B(E2; 2_2^+ \to 0_3^+)$ value measured previously and provides strong support for the 0_3^+ state as the band-head of the intruder configuration and for the shape coexistence in the semi-magic ^{116}Sn nucleus. IBM-2 calculations with mixing reproduce the experimental data very well, giving insight into the degree of mixing between the different states.

I. INTRODUCTION

The Sn isotopes have played a pivotal role in the development of our understanding of nuclear structure, particularly because they are some of the best examples of seniority structures in nuclei (see, e.g., Ref. [1]). Indeed, the near constancy of the 2_1^+ energies from $N = 52$ (^{102}Sn) to $N = 80$ (^{130}Sn) is remarkable. Another well documented phenomenon in the Sn isotopes is shape coexistence (see, e.g., Refs. [2–4]). The mid-shell nuclei near Z=50 exhibits shape coexisting phenomena similar to those of the mid-shell neutron-deficient nuclei near $Z = 82$ (see e.g., Ref. [3]) which are far from the stability line and therefore more difficult to study. State of the art experimental methods have been developed and successfully applied to the study of nuclei near $Z = 82$ (see e. g. [5, 6]).

The shape-coexisting bands in the mid-shell Sn isotopes, $^{112-118}$Sn, were first suggested by Brön *et al.* [7], based on the rotational-like structures observed in a series of (α, xn) reactions. Taking into account the observation of enhanced cross sections to the 0^+ band heads in $(^3He, n)$ reactions, where they were populated, in some cases, stronger than the ground states [8], Brön *et al.* [7]

suggested that they were built on intruding $2p - 2h$ proton excitations across the $Z = 50$ closed shell. Subsequent detailed spectroscopy using light-ion reactions and detecting both the γ-ray and conversion electron decays of the low-lying 0^+ and 2^+ levels, [9–11], provided firm evidence, summarized by Julin [12], for the deformed shapes of the intruder bands through the observation of enhanced $E0$ transitions.

Located at the neutron mid-shell, ^{116}Sn possesses the most comprehensive level scheme of the Sn isotopes. In addition to fusion-evaporation reactions [7, 13–16], its states have been studied by inelastic hadronic scattering reactions [17–22], electron scattering [19, 23], nuclear resonance fluorescence [24, 25], transfer reactions [8, 26–30], and $\beta^-/\beta^+/EC$ decay [31–34]. The most recent studies [33, 34], which included conversion electron spectroscopy from the β-decay of ^{116m1}In, suggested that while there was considerable mixing, the 0_3^+ state was the head of the intruder band, rather than the 0_2^+ state. This finding has important consequences, because it suggests that the band heads of the intruder bands of the other Sn isotopes may be the 0_3^+ states as well (see Fig. 1).

While the mid-shell Sn isotopes have been generally well studied, there are still significant gaps in our spectroscopic knowledge of their levels; in particular, the lifetimes of the 0_3^+ and 4_2^+ states assigned to the intruder bands are poorly known or only have limits determined,

* *Corresponding author*; petrache@csnsm.in2p3.fr

prohibiting to draw clear conclusions on the collectivity of the bands and their band heads. In the present paper, we report our determination of the lifetime of the 4_2^+, 2529-keV state of ^{116}Sn using the FIPPS array in conjunction with LaBr$_3$ ancillary detectors [35]. Moreover, we demonstrate the utility of the (n_{th}, γ) reactions for probing the non-yrast states and measuring of their lifetimes that often are in the range of 1 – 200 ps. Prior to this study, in which we report detailed *sd* IBM-2 calculations including mixing, there were limited theoretical calculations which could reproduce the mixing and the transition probabilities in ^{116}Sn.

II. EXPERIMENTAL DETAILS

The present (n_{th}, γ) measurement was performed using a 10 mg ^{115}Sn target with 50% enrichment, which assured that over 99% of the neutron capture events led to the isotope of interest, ^{116}Sn. The experiment was conducted at the colimated neutron guide of the FIPPS setup at the Institut Laue-Langevin (ILL) in Grenoble, France, with a thermal neutron flux of 10^8 n/(cm^2·s) at the target position. The detection setup consisted of 8 Ge-clover and 16 LaBr$_3$ scintillator detectors. Similar to the setup described in Ref. [35], the 8 Ge-clover detectors, each made of four high-purity Ge crystals, were arranged in a central ring around the target position, perpendicular to the beam axis. Forward and backward rings of 8 LaBr$_3$ detectors each were installed at an angle of 45° relative to the beam axis. In between each Ge-clover and LaBr$_3$ detector, 15-mm thick lead slides were installed to constitute a through-going 10-cm large ring of lead in order to protect the two detector types from inter-detector Compton scattering. No further shielding has been used. The cylindrical LaBr$_3$ crystals all have a diameter of 3.8 cm. The length of 8 crystals is 3.8 cm (installed in one ring), while the length of the other 8 crystals is 5.1 cm. The energy resolutions of the Ge and LaBr$_3$ detectors at 1.332 MeV were 0.19% and 2.7%, respectively. The singles counting rates achieved in this experiment were ~ 2 kHz and ~ 1.5 kHz, respectively. We collected 1.4×10^9 LaBr$_3$-Ge-Ge and 4.4×10^8 LaBr$_3$-LaBr$_3$-Ge coincidences in 6 days. The projections of triple-$\gamma\gamma\gamma$ coincidences are shown in Fig. 2, where the energies of the most important γ-ray transitions of ^{116}Sn are indicated.

The fast-timing setup at FIPPS

In order to perform sub-nanosecond lifetime measurements in neutron-capture reactions, the Ge-gated γ-γ fast-timing technique using LaBr$_3$ detectors was employed. The excellent energy resolution of the Ge detectors permits precise selection of a γ ray from a specific triple-$\gamma\gamma\gamma$ cascade and produces clean LaBr$_3$ coincidence spectra with few γ rays and reduced Compton background. The LaBr$_3$ detectors were used for time-difference measurements between the γ rays feeding and de-exciting an excited state with analog time-to-amplitude converters (TACs) as described in Refs. [38, 39]. The pre-amplified detector signals and the TAC output signals were directly connected to 250 MHz CAEN model 1730 digitizers. Time-stamped data were acquired and sorted offline to produce Ge-LaBr$_3$-Ge events for coincidence analysis and Ge-LaBr$_3$-LaBr$_3$-TAC events for lifetime determination.

The LaBr$_3$-LaBr$_3$-TAC coincidence data were used to construct a so-called symmetric energy−energy−time-difference cube, as is commonly done when using Ge detectors. The energy axes are symmetric under the exchange of E_1 and E_2, while the time-difference axis is anti-symmetric. A precise alignment of the time-difference spectra of 104 detector-detector combinations was implemented. Sixteen combinations were excluded from the analysis due to the presence of inter-detector Compton scattering (more details on this phenomenon can be found in Ref. [35]). The time alignment was performed in order to optimise the time resolution of the superimposed data collected by all detectors of the fast-timing array. With this simple procedure, the total γ-γ time-differences are incremented twice, in two identical mirror-symmetric time-difference distributions, with mirror-symmetric mean time-walk characteristics relative to a constant reference time, t_0 [39]. It should be stressed that this procedure is consistent with the generalized centroid difference method (described in Refs. [35, 40]) which cancels typical systematic shifts related to the geometry, long-term time drifts and the different individual timing responses of the detectors, as described and shown in Ref. [39]. The mean time-walk curve, $TW(E_\gamma)$ presented in Fig. 3, was determined using nearly background-free full-energy peak (FEP) events as obtained from measurements using a ^{152}Eu γ-ray source and the ^{48}Ti$(n_{th}, \gamma)^{49}$Ti reaction. The accuracy of the time-walk calibration is 3 ps and corresponds to a 2σ standard deviation. A detailed description of the γ-γ (FEP vs. FEP) time-walk calibration procedure is given in Ref. [39].

The time walk is needed for the determination of sub-nanosecond lifetimes using the well-known centroid-shift method [41, 42]. The centroid of a time-difference distribution $D(t)$ is given by the mean value of the time over the distribution as:

$$C[D(t)] = \frac{\sum_{t_{\min}}^{t_{\max}} t D(t)}{\sum_{t_{\min}}^{t_{\max}} D(t)}. \tag{1}$$

In order to avoid possibly large systematic errors related to the random coincidences on the left and the right of the time-difference distribution, the experimental integration limits, $t_{\min}$ and $t_{\max}$, are set just at the beginning and at the end of the tails of the time-difference distribution (see also Figs. 5 and 8 in section III). According to the centroid-shift method, the centroid of the anti-symmetrized time-difference distributions can be written
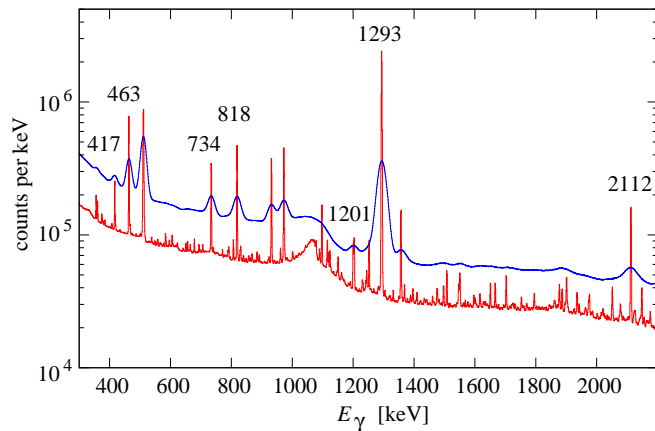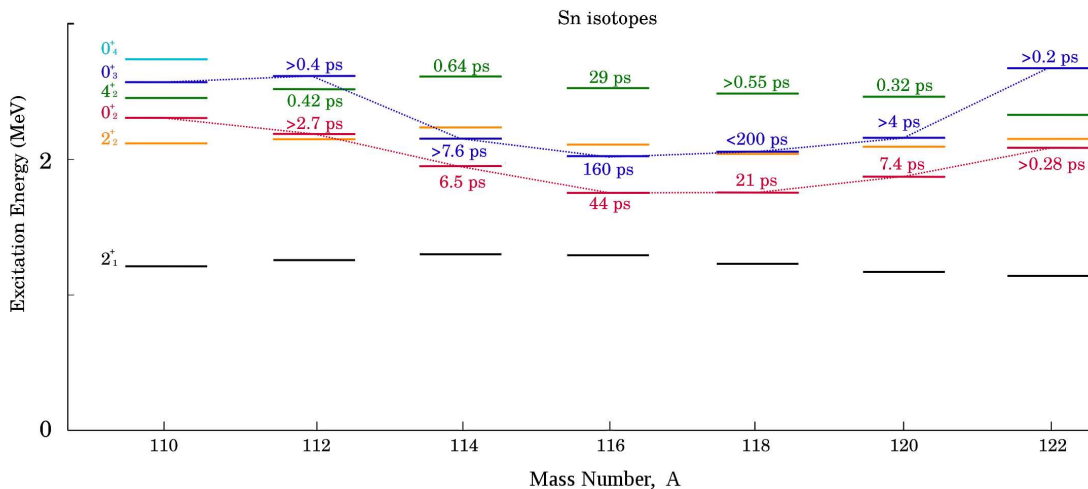
FIG. 1. Systematics of the Sn isotopes showing the half-lives or the limits of half-lives of the 0_2^+ (red), 0_3^+ (blue) and 4_2^+ (green) states. The half-lives are taken from Refs. [36, 37] and from this work.

FIG. 2. The projections of the FIPPS Ge and the fast-timing LaBr$_3$ γ-ray spectra from triple-$\gamma\gamma\gamma$ coincidences of the ^{115}Sn$(n_{th}, \gamma)^{116}$Sn reaction. While the Ge spectrum was generated using the LaBr$_3$-Ge-Ge events, the LaBr$_3$ spectrum is from the fast-timing LaBr$_3$-LaBr$_3$-Ge events. The Ge spectrum is scaled by a factor of 0.5 for illustrative comparison with the LaBr$_3$ spectrum.

FIG. 3. The mirror-symmetric mean time-walk characteristics of the FIPPS fast-timing array with 16 LaBr$_3$ detectors.

as [39]:

$$C_{\text{FEP}}(E_1, E_2) = t_0 + TW(E_1, E_2) + \text{sgn}(E_2)\tau, \quad (2)$$

where τ is the mean lifetime of the nuclear excited state and $\text{sgn}(E_2)$ is -1 for $E_2 = E_{\gamma_{\text{feeder}}}$ and $+1$ for $E_2 = E_{\gamma_{\text{decay}}}$. The subscript "FEP" indicates that no time-correlated Compton background is present. The present fast-timing data are corrected for the time walk using $TW(E_1, E_2) = TW(E_1) - TW(E_2)$ [39], as derived from
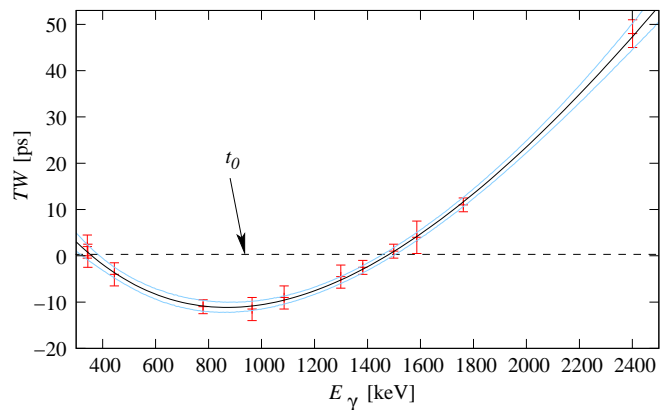
the curve shown in Fig. 3. Also, the reference time is adjusted to $t_0 = 0$. Then, the mean lifetime directly corresponds to the centroid $C_{\text{FEP}}(E_1 = E_{\gamma_{\text{feeder}}}, E_2 = E_{\gamma_{\text{decay}}})$.

III. LIFETIMES OF EXCITED STATES OF ^{116}SN

In total, lifetimes of five nuclear excited states of ^{116}Sn could be extracted form the experiment and the results are given in Tab. I. The results were derived without the subtraction of background of any kind. This data treatment is made in order not to possibly falsify the results and also to make it possible to precisely mea-

sure the timing properties of the FEP events as well as the time-correlated (coincident) Compton background events. The lifetime results were derived by employing an analytical Compton-background time correction using relative values, as proposed in Refs. [43–45]. As a good example for its application, we first present the lifetime measurement of the 0_3^+, 2027-keV state. This level lifetime has already been measured to be 231(29) ps [46]. Subsequently, also the determination of the 4_2^+ level lifetime will be presented.

The lifetime of the 0_3^+, 2027-keV state

As can be seen in Fig. 2, the γ-ray spectrum of ^{116}Sn is too complex for γ-γ time-difference measurements using LaBr$_3$-LaBr$_3$ coincidences only. Therefore, the Ge detectors are used in coincidence for precise selection of a γ ray to considerably clean the LaBr$_3$ coincidence spectra, in our case, the $2_1^+ \rightarrow 0_1^+$, 1293-keV ground-state transition. An additional LaBr$_3$ gate set on γ_{feeder} or γ_{decay} allows us to investigate possible γ rays which may contaminate the peaks of interest. This procedure is performed with Ge-LaBr$_3$-Ge coincidences. Fig. 4 (upper panel) shows the result of this analysis for the de-exciting $0_3^+ \rightarrow 2_1^+$, 734-keV γ-ray transition. In this case, the resulting doubly-gated γ-ray spectrum is extremely clean and the FEP at 734 keV is well separated from other peaks. A similar result has been obtained for the feeding $2^+ \rightarrow 0_3^+$, 1201-keV γ ray, as shown in the lower panel of Fig. 4. Thus, the Ge(1293)-triggered 1201-734-keV time-difference spectrum could be generated and the result is presented in Fig. 5. First, a significant exponential decay of the 1201-734-keV time distribution is observed. A convolution fit assuming a Gaussian prompt time distribution has been performed as well as a centroid determination. We would like to point out that the lifetime determination via the centroid measurement is most precise, but also most sensitive to Compton-background contributions to the experimental time distribution. As the results using the two methods are not consistent, this clearly indicates non-negligible Compton-background contributions.

In order to properly remove the time contributions of the Compton background, we used an analytical background time correction, which has been shown to be most reliable [43–45]:

$$C_{\text{FEP}} = C_{\text{exp}} + \frac{1}{2}[t_{\text{cor}}(E_{\text{feeder}}) + t_{\text{cor}}(E_{\text{decay}})] \qquad (3)$$

with

$$t_{\text{cor}} = \frac{C_{\text{exp}} - C_{\text{BG}}}{\text{P/B}}. \qquad (4)$$

P/B is the peak-to-background ratio and C_{BG} is the centroid of the background time distribution at the considered γ-ray energy. As C_{BG} cannot be measured directly,
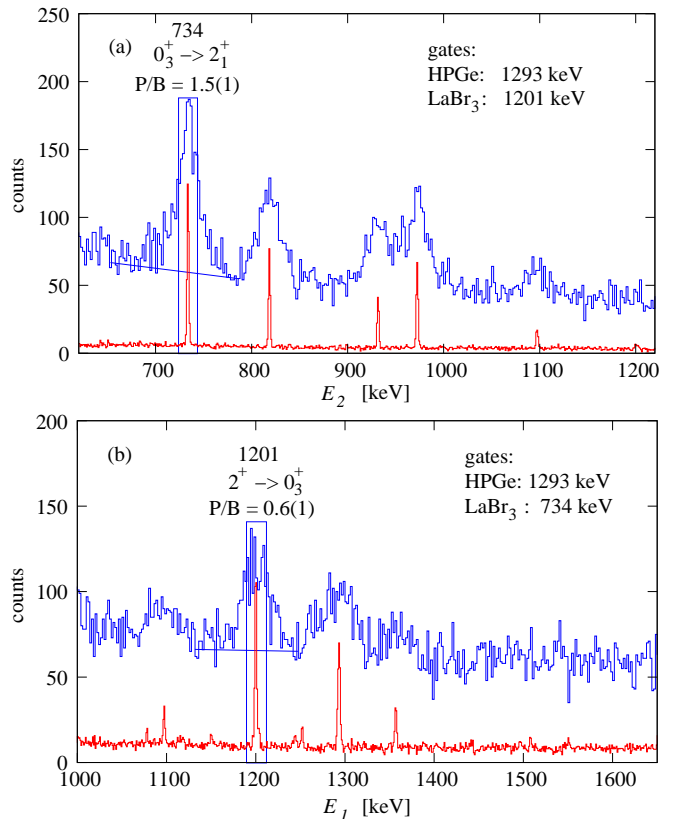

FIG. 4. Doubly-gated Ge and LaBr$_3$ coincidence spectra generated using gates as indicated and illustration of the determination of the relative full-energy peak to Compton-background ratio, P/B. The spectra were derived from triple Ge-LaBr$_3$-Ge and respective Ge-LaBr$_3$-LaBr$_3$ coincidences with a coincidence window of 250 ns.

it is interpolated from centroid measurements of several background time spectra, generated at different energies around the FEP of interest. The possible systematic error of the determination of C_{BG} is derived from the 1σ uncertainty band by analyzing the correlation matrix. The background time response analyses are presented in Fig. 6, where the derived Compton time walk is shown to be smooth. As can be seen in Fig. 4, no sudden increase of the Compton background is observed over a large energy region around the FEPs of interest which explains the smoothness of the Compton time walk. It should be noted that the time response (C_{BG}) and the full width at half maximum (FWHM) of the two background components are dependent on the energy and are generally different.

In summary, the values given in Fig. 6 are inserted to Eqs. 2, 3 and 4 (with $t_0 = 0$ and $TW = 0$) and the lifetime for the 2027-keV, 0_3^+ state of ^{116}Sn of $\tau = 236(14)$ ps is obtained. The experimental uncertainty follows from error propagation and includes possible systematic errors. Our final result confirms the experimental result given in Ref. [46] while the precision has been improved by factor two.
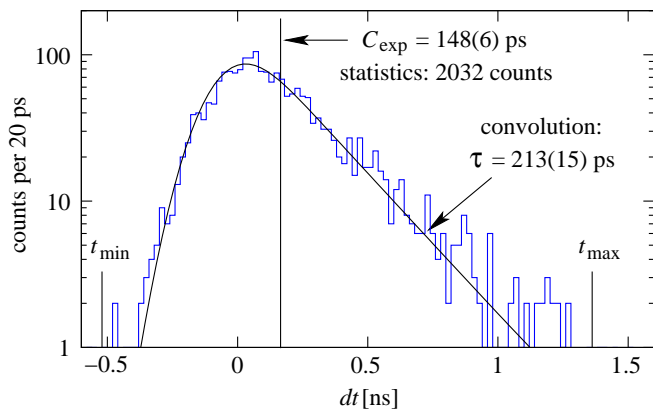
FIG. 5. The experimental time distribution of the 0_3^+ state of ^{116}Sn using the 1201-734-keV γ-γ cascade and the following 1293-keV γ ray employing the FIPPS Ge detectors as a trigger. The data are time-walk corrected and the reference time is $t_0 = 0$. The experimental centroid is determined using Eq. 1 and is indicated by the vertical line. The results are discussed in the text.

The lifetime of the 4_2^+, 2529-keV state

For the determination of the lifetime of the 4_2^+, 2529-keV state of ^{116}Sn, we investigated its decay by the 417-keV, $4_2^+ \rightarrow 2_2^+$ γ ray. The most intense γ ray directly feeding the 4_2^+ state is the 467-keV γ ray from the 2996-keV, 3_1^+ state. However, this γ ray is in coincidence with the 463-keV, $0_2^+ \rightarrow 2_1^+$ transition, which has an intensity more than 50 times larger. Such close-lying γ rays cannot be resolved with LaBr$_3$ detectors, which have limited energy resolution. As can be seen in Fig. 7, the 463-keV γ-ray peak has been completely eliminated by gating on the parallel $2_2^+ \rightarrow 0_1^+$, 2112-keV γ ray using the FIPPS clover detectors. The resulting doubly-gated coincidence spectrum, using an additional LaBr$_3$ gate set on γ_{decay}, is clean and the peaks are well separated. Note that (n_{th}, γ) reactions always produce a 511-keV annihilation line due to the presence of coincident "primary" γ rays with energies of a few MeV depopulating the neutron-capture state at about 8 MeV.

The experimental time-difference distribution of the 467-417-keV γ_{feeder}-γ_{decay} cascade triggered by the 2112-keV γ ray using the clover detectors, is presented in Fig. 8. The time peak corresponds to the total statistics and includes Compton-background events. In this case, only a small analytical time correction of $+7(10)$ ps for the total Compton-background contributions has been derived as described before. The final result for the lifetime of the 2529-keV, 4_2^+ state of ^{116}Sn is $\tau = 42(14)$ ps (half-life $T_{1/2} = 29(10)$ ps). The relatively large experimental uncertainty is mainly determined by the statistics. One should note that the value obtained for the 4_2^+ state of ^{116}Sn is significantly larger than that of the 4_1^+ state, which has been measured by Coulomb excitation as $T_{1/2}=0.47(9)$ ps, while the value adopted by NNDC is
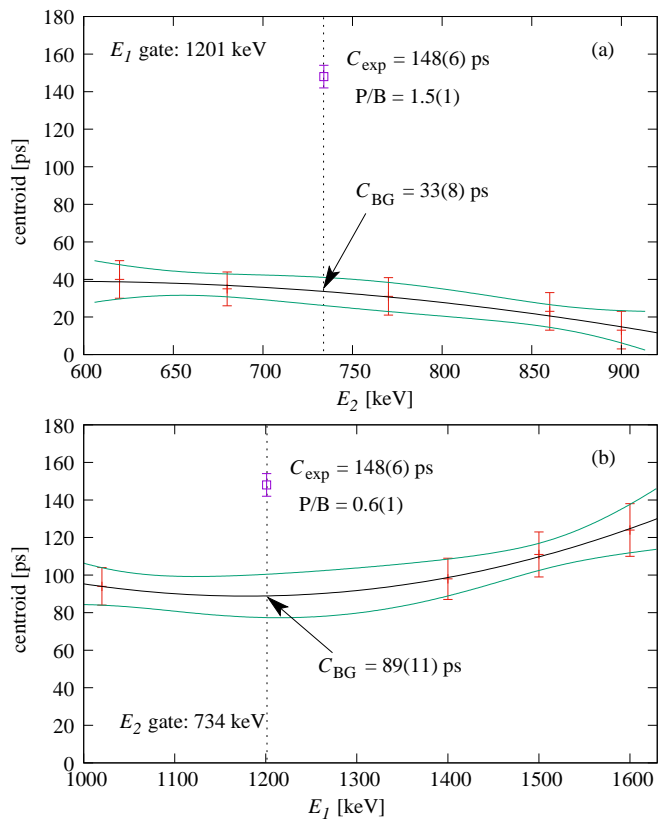

FIG. 6. Interpolation of the time response C_{BG} of the Compton background at $E_{\text{decay}} = 734$ keV (upper panel) and at $E_{\text{feeder}} = 1201$ keV (lower panel). The data are corrected for the time walk as derived from Fig. 3 and are fitted using a second order polynomial. The green lines represent the $1\,\sigma$ uncertainty bands obtained by analyzing the correlation matrices.

$T_{1/2}=0.28(14)$ ps [36], which leads to a $B(E2; 4_1^+ \rightarrow 2_1^+)$ value of 38(9) W. u., nearly twice the 22(4) W. u. value deduced from the Coulomb excitation measurement. The $B(E2; 4_1^+ \rightarrow 2_1^+)$ value of 22(4) W. u. is closer to the adopted values of 17(3) W. u. and 5.9(5) W. u. for the neighboring nuclei ^{118}Sn and ^{114}Sn, respectively. We therefore adopt the $T_{1/2}=0.47(9)$ ps half-life for the 4_1^+ state of ^{116}Sn, which better fits the systematics in the sequence of Sn nuclei.

Further known half-lifes could be measured and the results are listed in Tab. I. For the cases with $T_{1/2} \lesssim 50$ ps, the total background time correction was smaller than 10 ps. This is in agreement with the observations reported in Refs. [43–45]. The given experimental uncertainty includes the statistical error and the uncertainties of the time-walk and the background-time corrections. In many cases, the major contribution is determined by the statistics. For the lifetime determination of the 0_2^+ state, the weighted average value of the results using three different E_{feeder} gates is given in Tab. I.
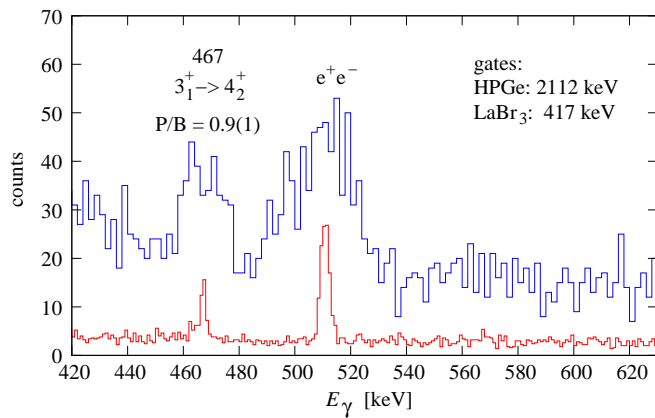
FIG. 7. Doubly gated coincidence γ-ray spectra generated to investigate the quality of the spectrum around the 467-keV FEP and the peak-to-background ratio (P/B) of the LaBr$_3$ spectrum.
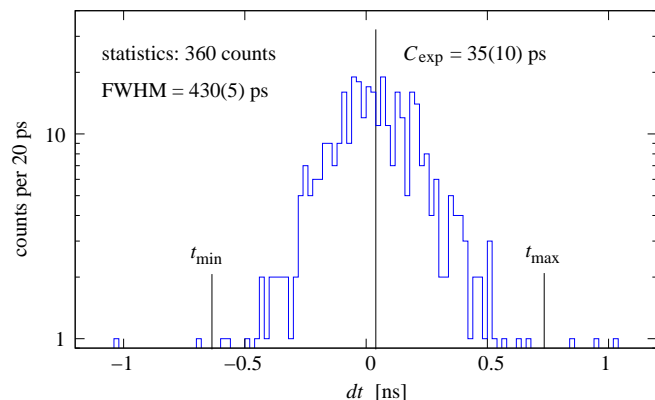

FIG. 8. The Ge(2112 keV)-triggered time-difference distribution between the 467- and 417-keV transitions feeding and and de-exciting the 4_2^+ state of ^{116}Sn. The result is time-walk corrected relative to $t_0 = 0$.

IV. DISCUSSION

DETAILS OF THE CALCULATION

To test the mixing hypothesis between the normal and intruder configurations, we performed sd IBM-2 calculations using the computer code NPBOS [47]. As has been recently done for ^{114}Sn [37], we chose the IBM-2 parameters determined for the $N = 66$ isotone ^{112}Pd to describe the proton 2p-2h intruder configuration in ^{116}Sn using the same Hamiltonian for our calculations. However, we adjusted the $C_{4\rho}$ parameter of the residual nucleon-nucleon interaction in the Hamiltonian [48] to -0.15 as compared to 0.10 [49]. This change is one possible way to move the intruder 4_2^+ state closer to the 4_1^+ state of the normal configuration. We note that changing this parameter to a smaller value than the one previously determined also improves the position of the 6_1^+ state of ^{112}Pd, which was not known at the time of the IMB-

TABLE I. Experimental half-lifes of nuclear excited states of ^{116}Sn derived using the Ge-gated γ-γ fast-timing technique from the ^{115}Sn$(n_{th}, \gamma)^{116}$Sn reaction performed at the FIPPS setup of the ILL in combination with 16 LaBr$_3$ scintillator detectors.

state J^π	Ge gate [keV]	LaBr$_3$ gates E_1-E_2 [keV]	$T_{1/2}$ [ps] exp.	$T_{1/2}$ [ps] lit.
2_1^+	417	818-1293	≤ 6	$0.37(2)^*$
0_2^+	1293	2148-463	56(17)	
	1293	2244-463	48(15)	
	1293	2357-463	51(14)	
		w. average:	51(12)	$45(10)^\dagger$
0_3^+	1293	1201-734	164(10)	$160(20)^\dagger$
2_2^+	1293	417-818	≤ 7	$1.89(10)^\ddagger$
4_2^+	2112	467-417	29(10)	$< 100^\dagger$

* average of 5 values [36], † from Ref. [46], ‡ from Ref. [36]

2 study of Ref. [49]. To find a suitable set of parameters for the normal configuration in ^{116}Sn, we used the parameters determined in our previous study of ^{114}Sn as a basis [37]. The following parameters were determined for ^{116}Sn: $\varepsilon_\nu = 1.30$ MeV, $C_{0\nu} = -0.75$ MeV, $C_{2\nu} = 0$ MeV, $C_{4\nu} = -0.11$ MeV, $\kappa_{\nu\nu,1} = -0.0002$, $\chi_{\nu,1} = -0.005$ (see Ref. [48] for a description of th sd IMB-2 Hamiltonian and its parameters). The two configurations, intruder and normal, are calculated separately, and subsequently admixed by the mixing operator as defined in Ref. [50–52]. The two parameters of this mixing operator were set to $\alpha = \beta = 0.08$ MeV, i.e., similar to those found for the Cd isotopes in Ref. [52], and the relative energy shift Δ between the normal and intruder configurations was chosen as 2.45 MeV. After mixing, electromagnetic transitions rates can be calculated. We obtained good agreement with known absolute $E2$ transition strengths and $B(E2)$ γ-ray branching ratios using the following parameters for the $E2$ transition operator [50–52]: $e_\nu = 0.07$ eb^2, $e_\pi = 0.161$ eb^2 and $e_2/e_0 = 1.436$. These parameters are also similar to what was found in ^{114}Sn [37] and the Cd isotopes [52].

DISCUSSION OF THE RESULTS

From the experimental data, it can be concluded that there is strong mixing between the normal and intruder configurations of ^{116}Sn. This conclusion is based on the observation of enhanced $B(E2; 2_2^+ \rightarrow 0_{2,3}^+)$ and $B(E2; 4_{1,2}^+ \rightarrow 2_2^+)$, with each having a value of several tens of Weisskopf units. The present calculations can describe these experimental observations fairly well (see Fig. 9 and Table II). From the mixed wave functions predicted by the present calculations, strong mixing between the 0_2^+ and 0_3^+ states and for the 4_1^+ and 4_2^+ states, is indeed observed. Large amplitudes of normal $|2\rangle$ and intruder $|\bar{1}\rangle$ components for the 0_2^+ and 0_3^+ states, and of $|1\rangle$ and $|\bar{1}\rangle$ components for the 4_1^+ and 4_2^+ states, respectively
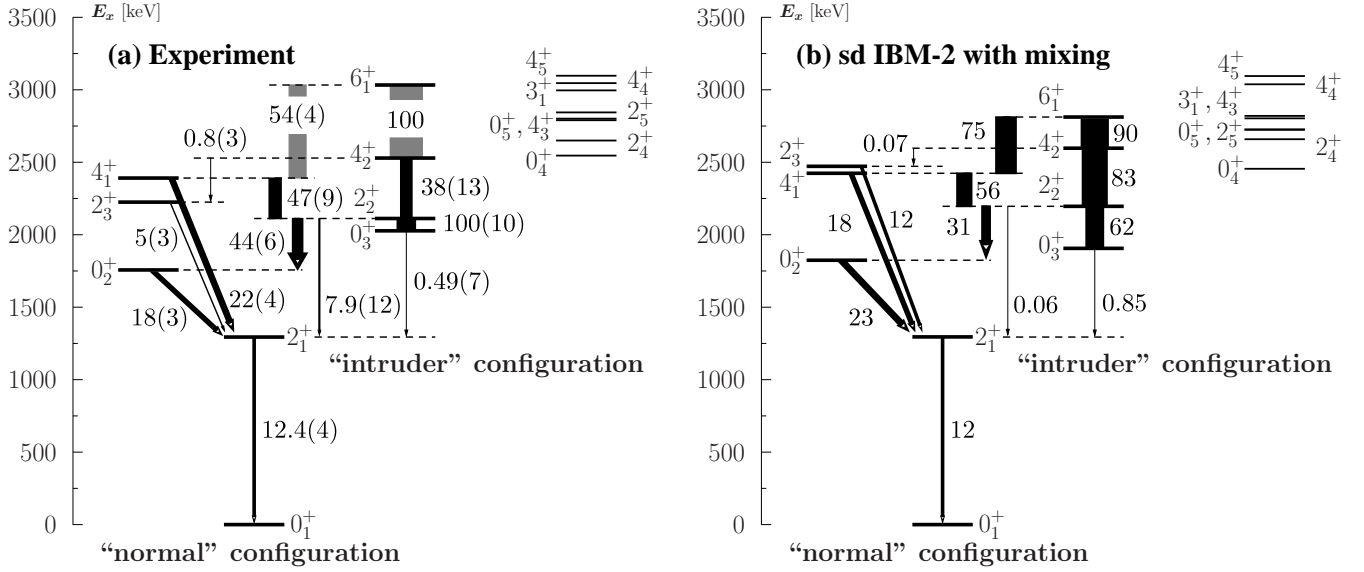
FIG. 9. Comparison of the absolute $B(E2)$ transition probabilities of the normal and intruder configurations identified experimentally in ^{116}Sn with the predictions of the sd IBM-2 with mixing. Additional low-spin states are shown up to 3 MeV. The experimental data has been taken from Refs. [33, 34, 36]. The transitions de-exciting the experimental 6_1^+ state are drawn with grey color to emphasize that only the γ-ray branching ratio is measured, not the absolute $B(E2)$ values as in the case of the other transitions.

(see Table III). The 0_2^+ and 4_1^+ states have dominant contributions from the corresponding normal configuration, i.e., eigenstates $|2\rangle$ and $|1\rangle$ of the corresponding spin, respectively, but also significant admixtures from the first intruder state of the same spin, i.e. the intruder wave function $|\bar{1}\rangle$. On the contrary, the intruder eigenstate $|\bar{1}\rangle$ constitutes the dominant part of the 0_3^+ wave function, but also a significant admixture of the first excited 0^+ state of the normal configuration, i.e. $|2\rangle$, is observed. All other contributions are negligible for those states.

In contrast to the $J^\pi = 0^+$ and $J^\pi = 4^+$ states, there is little mixing between the 2_2^+ and 2_3^+ states in the present model calculations. This shows that the corresponding selection rules for states to mix [53, 54] remain valid for the chosen parameters, i.e., $\Delta L = 0$ and $\nu = \tau$. Here, no mixing between the $2_{1,\text{intr.}}^+$ ($\tau = 1$) and $2_{2,\text{norm.}}^+$ ($\nu = 2$) states is possible. Instead, it is the $2_{2,\text{intr.}}^+$ ($\tau = 2$) and $2_{2,\text{norm.}}^+$ ($\nu = 2$) corresponding to the 2_3^+ and 2_4^+ states which will mix (see Table III). The large $B(E2; 2_2^+ \to 2_1^+) = 7.7(8)$ W.u. of the 819-keV transition, which cannot be reproduced by the present calculations, implies that some mixing between the underlying configurations of the 2^+ states is missing. We do, however, note that good agreement was achieved for most of the other absolute $B(E2; 2_2^+ \to J_f^\pi)$ and $B(E2; 2_3^+ \to J_f^\pi)$ values, see Table II. The complexity of the calculations still requires a more thorough test of the predicted wave functions. As can be seen in Fig. 9, the agreement for higher-lying excited states of a given spin is fairly good in terms of excitation energy. Many $B(E2)$ γ-ray branching ratios are known for those states

and have been compiled in Table IV, where they are compared with the model predictions. The experimental γ-ray branching ratios observed for the 0_4^+ and 2_4^+ states are in very good agreement with the IBM-2 predictions. Both states correspond to excited states of the normal configuration, see Table III. Also, the agreement for the tentatively assigned 0_5^+ state is fairly good; small experimental ratios are also small in the model and its decay is stronger to the 2_2^+ state than to the 2_3^+ state. The 0_5^+ state corresponds to an intrinsic excitation of the intruder configuration.

The $B(E2)$ γ-ray branching ratios calculated for the 4_3^+ state in comparison to the experimental quantities suggest that certain parts of the wave function are missing. Especially the decay intensities to the 2_1^+ and 2_2^+ are underestimated. In the model, the 4_3^+ state corresponds to the second eigenstate with $J^\pi = 4^+$ of the intruder configuration and has only negligible admixtures of other components. As already mentioned earlier, the intruder configuration with an $R_{4/2}$ ratio of 2.4 seems to obey mixing and $E2$ selection rules of the O(6) symmetry. Within this symmetry $E2$ decays to the first 2^+ state are forbidden while decays to the first 4^+ state are allowed due to the $\Delta\sigma = 0$ and $\Delta\tau \pm 1$ $E2$ selection rule. The small experimental $R(E2)_{2_2^+/4_2^+}$ ratio might support this interpretation. However, the calculated $R(E2)_{4_1^+/4_2^+}$ ratio could indicate that the mixing between the two lowest 4^+ states is overestimated, while mixing between the two lowest-lying 2^+ states is missing.

The comparison between the experimental and calculated branching ratios for the 3_1^+, 6_1^+, 4_4^+ and 4_5^+ basically

TABLE II. Comparison of the normal and intruder configurations identified experimentally with the predictions of the sd IBM-2 calculations with mixing in ^{116}Sn. If not specified otherwise, the experimentally determined γ-decay branching ratios have been taken from Ref. [33], the electron conversion coefficients from Ref. [34], and the level lifetimes from Ref. [36]. Multipole-mixing ratios have been taken from Refs. [34, 36]. To calculate the upper limits for the $2_3^+ \to 0_3^+, 2_2^+$ transitions, the γ-decay intensities of Ref. [36] were used. The new lifetime of the 4_2^+ level was determined in this work.

$J_i^\pi \to J_f^\pi$	E_x [MeV]	$E_{x,\text{IBM}}$ [MeV]	$B(E2)_{\text{exp.}}$ [W.u.]	$B(E2)_{\text{IBM}}$ [W.u.]
normal configuration				
$2_1^+ \to 0_1^+$	1.29	1.29	12.4(4)	12
$4_1^+ \to 2_1^+$	2.39	2.42	22(4)	18
$\to 2_2^+$			47(9)	56
$0_2^+ \to 2_1^+$	1.76	1.82	18(3)	23
$2_3^+ \to 0_1^+$	2.23	2.47	0.04(3)	0.002
$\to 2_1^+$			5(3)	12
$\to 0_2^+$			1.5(8)	0.10
$\to 0_3^+$			< 3	0.12
$\to 2_2^+$			< 6	93
intruder configuration				
$0_3^+ \to 2_1^+$	2.03	1.91	0.49(7)	0.85
$2_2^+ \to 0_1^+$	2.11	2.20	0.12	0.16
$\to 2_1^+$			7.9(12)	0.06
$\to 0_2^+$			44(6)	31
$\to 0_3^+$			100(10)	62
$4_2^+ \to 2_1^+$	2.53	2.60	0.00034(12)	4
$\to 2_2^+$			38(13)	83
$\to 2_3^+$			0.8(3)	0.07
$\to 4_1^+$			22^{+34}_{-20}	2
$6_1^+ \to 4_1^+$	3.03	2.81		75
$\to 4_2^+$				90
$\to 4_3^+$				0.07

follows this discussion, and the quantities and discrepancies can be understood by considering the $B(E2)$ selection rules of the O(6) symmetry as well. We note that despite the absolute values and some exceptions, i.e. for the 3_1^+ and $4_{3,4,5}^+$ states (see Table IV), the present calculations describe the general $B(E2)$ trends. Still, it needs to be mentioned that a different choice of $\chi_{\nu,i}$ for the normal and intruder configurations in the Hamiltonian and of the $B(E2)$ operator could probably improve the overall agreement. A $\chi_{\nu,1}$ value of -0.63 in contrast to the chosen -0.005 value for the normal configuration improves the agreement for the 2_5^+ and 4_5^+ branching ratios which were mentioned above. At the same time, the calculated $B(E2)$ branching ratio for the 0_4^+ state would be off by a factor of 10. The variation of $\chi_{\nu,1}$ has little impact on the excitation energies due to the small value of $\kappa_{\nu\nu,1}$.

Altogether, the comparison of the experimental data with the IBM-2 results seems to imply that besides the states of the normal and intruder configurations, which are normally discussed, intrinsic excitations of both configurations coexist at comparably low excitation energies in ^{116}Sn. The agreement with experimental data is fairly good considering the proton magicity of ^{116}Sn. One should, however, be very careful when considering the "normal" and "intruder" states in ^{116}Sn. Even though the states as arranged in Fig. 9 might have dominant contributions of the stated configuration, the real eigenstates of the individual Hamiltonians are strongly mixed with the other configuration as shown in Table III. Still, as noted in Ref. [33] and predicted by the present calculations, the 0_3^+ state corresponds to the bandhead of the "intruder" structure in ^{116}Sn. Similar conclusions were drawn for ^{114}Sn [37]. More data on the $2_{\text{intr.}}^+ \to 0_i^+$ transitions are needed in the other Sn isotopes for a better understanding of the intruder bands and to draw a firmer conclusion. The preliminary, but tempting, trend of an increasing Δ from 2.45 MeV for ^{116}Sn to 2.78 MeV for ^{114}Sn [37] should not be interpreted as a clear signature that the band-heads of the intruder bands are the 0_3^+ states, as long as the $B(E2; 2_{\text{intr.}}^+ \to 0_3^+)$ values are not known in other Sn nuclei. Future experiments are needed to clarify the mixing and the nature of the excited $0^+, 2^+, 4^+$ and 6^+ states in the magic Sn isotopes.

TABLE III. The mixed sd IBM-2 wave functions for the states shown in Tables II and IV. $|i\rangle$ and $|\bar{i}\rangle$ correspond to the ith state with a given J^{π} of the normal ($N_{\pi} = 0$) and intruder ($N_{\pi} = 2$) configurations, respectively.

| J^{π} | $N_{\pi} = 0$ | | | | $N_{\pi} = 2$ | | | |
	$|1\rangle$	$|2\rangle$	$|3\rangle$	$|4\rangle$	$|\bar{1}\rangle$	$|\bar{2}\rangle$	$|\bar{3}\rangle$	$|\bar{4}\rangle$
0_1^+	0.9984	-0.0004	0.0000	0.0001	-0.0538	0.0158	-0.0058	0.0000
0_2^+	-0.0281	0.8416	0.0000	-0.0070	-0.5351	-0.0613	0.0285	0.0002
0_3^+	-0.0459	-0.5341	-0.0006	-0.0048	-0.8430	0.0390	-0.0184	-0.0001
0_4^+	0.0001	-0.0009	1.0000	-0.0008	-0.0005	-0.0065	0.0026	0.0002
0_5^+	0.0155	-0.0719	-0.0066	-0.2696	0.0012	-0.9596	0.0314	0.0004
2_1^+	0.9948	0.0000	-0.0016	0.0001	-0.1000	-0.0086	0.0142	-0.0065
2_2^+	-0.0998	0.0184	-0.0618	-0.0011	-0.9892	0.0046	-0.0050	0.0028
2_3^+	0.0084	0.5474	0.0122	0.0001	0.0113	0.8365	0.0029	-0.0022
2_4^+	0.0034	-0.8365	0.0127	-0.0001	-0.0148	0.5473	-0.0022	0.0024
2_5^+	-0.0085	0.0039	0.9672	0.0078	-0.0588	-0.0164	0.2182	-0.1115
3_1^+	0.0822	0.0064	-0.0219	0.0005	-0.9964	0.0008	-0.0011	0.0010
4_1^+	0.7769	-0.0007	-0.0195	-0.0035	0.6288	-0.0243	0.0012	-0.0071
4_2^+	-0.6282	-0.00011	-0.0286	-0.0051	0.7767	0.0340	-0.0013	0.0084
4_3^+	-0.0402	-0.0005	-0.0068	-0.0010	0.0109	-0.9991	-0.0002	0.0010
4_4^+	0.0017	0.0006	0.0001	-0.0001	-0.0003	0.0001	-1.0000	-0.0001
4_5^+	0.0000	-0.9998	0.0006	0.0002	-0.0012	0.0004	-0.0006	-0.0177
6_1^+	0.1061	0.0078	-0.0255	0.0445	0.9930	-0.0076	0.0004	-0.0010

TABLE IV. Comparison of experimentally determined $B(E2)$ γ-ray branching ratios for states not shown in Table II with the predictions of the sd IBM-2. The 6_1^+ state has been added to the comparison as well. The experimental data were taken from Refs. [33, 36].

$J_i^\pi \to J_{f,1}^\pi, J_{f,2}^\pi$	E_x [MeV]	$E_{x,\text{IBM}}$ [MeV]	$R(E2)_{\text{exp.}}$	$R(E2)_{\text{IBM}}$
$0_4^+ \to 2_1^+, 2_2^+$	2.44	2.55	0.17(6)	0.14
$2_4^+ \to 2_1^+, 2_2^+$	2.66	2.65	0.35(7)	0.24
$(0_5^+) \to 2_1^+, 2_2^+$	2.71	2.79	0.028(3)	$5.7 \cdot 10^{-4}$
$\to 2_1^+, 2_3^+$			0.055(8)	$8.9 \cdot 10^{-4}$
$\to 2_2^+, 2_3^+$			2.0(4)	1.6
$4_3^+ \to 2_1^+, 2_2^+$	2.80	2.82	1.12(7)	0.0003
$\to 4_1^+, 4_2^+$			0.069(4)	0.69
$\to 2_1^+, 4_1^+$			6.2(3)	$1.1 \cdot 10^{-5}$
$\to 2_2^+, 4_2^+$			0.112(7)	0.03
$2_5^+ \to 0_1^+, 2_1^+$	2.84	2.73	0.07(2)	0.78
$3_1^+ \to 2_1^+, 2_3^+$	3.00	2.81	0.044(7)	$3.2 \cdot 10^{-6}$
$\to 4_1^+, 4_2^+$			0.25(8)	0.81
$\to 2_1^+, 4_1^+$			0.025(6)	$1.7 \cdot 10^{-5}$
$\to 2_3^+, 4_2^+$			0.15(4)	4.4
$6_1^+ \to 4_1^+, 4_2^+$	3.03	2.81	0.54(4)	0.78
$4_4^+ \to 2_1^+, 4_1^+$	3.05	3.04	2.29(9)	0.0007
$\to 2_1^+, 4_2^+$			0.33(3)	0.002
$\to 2_1^+, 2_4^+$			0.26(2)	0.0003
$\to 2_4^+, 4_1^+$			8.7(6)	3.5
$\to 2_4^+, 4_2^+$			1.3(2)	12.2
$\to 2_4^+, 4_3^+$			0.035(2)	0.003
$\to 4_1^+, 4_2^+$			0.14(2)	3.5
$\to 4_1^+, 4_3^+$			0.0040(2)	0.0009
$4_5^+ \to 4_1^+, 4_2^+$	3.10	3.08	2.7(2)	0.0003
$\to 4_1^+, 4_3^+$			0.72(9)	$6.2 \cdot 10^{-5}$
$\to 4_2^+, 4_3^+$			0.27(13)	0.22
$\to 2_3^+, 2_4^+$			0.14(2)	2.3

[1] I. Talmi, Phys. Scr. **92**, 083001 (2017).

[2] J. Wood, K. Heyde, W. Nazarawicz, M. Huyse, and P. van Duppen, Phys. Rep. **215**, 103 (1992).

[3] K. Heyde and J. L. Wood, Rev. Mod. Phys. **83**, 1467 (2011).

[4] P. E. Garrett, J. Phys. G **43**, 084002 (2016).

[5] N. Bree *et al.*, Phys. Rev. Lett. **112**, 162701 (2014).

[6] R. Julin, T. Grahn, J. Pakarinen, and P. Rahkila, J. Phys. G **43**, 024004 (2016).

[7] J. Brön, W. H. A. Hesselink, A. Van Poelgeest, J. J. A. Zalmstra, M. J. Uitzinger, H. Verheul, K. Heyde, M. Waroquier, H. Vincx, and P. Van Isacker, Nucl. Phys. A **318**, 335 (1979).

[8] H. W. Fielding, R. E. Anderson, C. D. Zafiratos, D. A. Lind, F. E. Cecil, H. H. Wieman, and W. P. Alford, Nucl. Phys. A **281**, 389 (1977).

[9] J. Kantele, R. Julin, M. Luontama, A. Passoja, T. Poikolainen, A. Bäcklin, and N. G. Jonsson, Z. Physik A **289**, 157 (1979).

[10] A. Bäcklin, N. G. Jonsson, R. Julin, J. Kantele, M. Luontama, A. Passoja, and T. Poikolainen, Nucl. Phys. A **351**, 490 (1980).

[11] N. G. Jonsson, A. Bäcklin, J. Kantele, R. Julin, M. Luontama, and A. Passoja, Nucl. Phys. A **371**, 333 (1981).

[12] R. Julin, Phys. Scr. **T56**, 151 (1995).

[13] A. Van Poelgeest, J. Bron, K. Hesselink, W. H. A. Allaart, J. J. A. Zalmstra, M. J. Uitzinger, and H. Verheul, Nucl. Phys. A **346**, 70 (1980).

[14] S. Lunardi, P. J. Daly, F. Soramel, C. Signorini, B. Fornal, G. Fortuna, A. M. Stefanini, R. Broda, W. Meczynski, and J. Blomqvist, Z. Phys. A **328**, 487 (1987).

[15] M. B. Chatterjee, P. Banerjee, B. K. Sinha, S. Bose, R. Bhattacharya, and S. K. Basu, Phys. Rev. C **42**, 2737 (1990).

[16] A. Savelius, S. Juutinen, K. Helariutta, P. Jones, R. Julin, P. Jamsen, M. Muikku, M. Piiparinen, J. Suhonen, S. Tormanen, R. Wyss, P. T. Greenlees, P. Simecek, and D. Cutoiu, Nucl. Phys. A **637**, 491 (1998).

[17] O. Beer, A. El Behay, P. Lopato, Y. Terrien, G. Vallois, and K. Seth, Nucl. Phys. A **147**, 326 (1970).

[18] H. Wienke, H. P. Blok, and J. Blok, Nucl. Phys. A **405**, 237 (1983).

[19] S. Y. Van Der Werf, N. Blasi, M. N. Harakeh, G. Wenes, A. D. Bacher, G. T. Emery, C. W. Glover, W. P. Jones, H. J. Karwowski, H. Nann, C. Olmer, P. Den Heijer, C. W. De Jager, H. De Vries, J. Ryckebusch, and M. Waroquier, Phys. Lett. B **166**, 372 (1986).

[20] G. Bruge, J. C. Faivre, H. Faraggi, and A. Bussiere, Nucl. Phys. A **146**, 597 (1970).

[21] J. M. Moss, D. R. Brown, D. H. Youngblood, C. M. Rozsa, and J. D. Bronson, Phys. Rev. C **18**, 741 (1978).

[22] S. Raman, T. A. Walkiewicz, S. Kahane, E. T. Jurney, J. Sa, Z. Gácsi, J. L. Weil, K. Allaart, G. Bonsignori, and J. F. Shriner, Phys. Rev. C **43**, 521 (1991).

[23] J. W. Lightbody Jr., S. Penner, S. P. Fivozinsky, P. L. Hallowell, and H. Crannell, Phys. Rev. C **14**, 952 (1976).

[24] K. Govaert, L. Govor, E. Jacobs, D. De Frenne, W. Mondelaers, K. Persyn, U. Yoneama, M. L. andKneissl, J. Margraf, H. H. Pitz, K. Huber, S. Lindenstruth, R. Stock, K. Heyde, A. Vdovin, and V. Y. Ponomarev, Phys. Lett. B **335**, 113 (1994).

[25] K. Govaert, F. Bauwens, J. Bryssinck, D. De Frenne, E. Jacobs, W. Mondelaers, L. Govor, and V. Y. Ponomarev, Phys. Rev. C **57**, 2229 (1998).

[26] E. Schneid, A. Prakash, and B. Cohen, Phys. Rev. **156**, 1316 (1967).

[27] K. Yagi, Y. Saji, Y. Ishimatsu, T. andIshizaki, M. Matoba, Y. Nakajima, and C. Y. Huang, Nucl. Phys. A **111**, 129 (1968).

[28] J. M. Schippers, J. M. Schreuder, S. Y. van der Werf, K. Allaart, N. Blasi, and M. Waroquier, Nucl. Phys. A **510**, 70 (1990).

[29] J. M. Schippers, W. T. A. Borghols, M. A. Hofstee, R. F. Noorman, J. M. Schreuder, S. Y. van der Werf, and N. Blasi, Nucl. Phys. A **548**, 271 (1992).

[30] P. Guazzoni, L. Zetta, A. Covello, A. Gargano, B. F. Bayman, T. Faestermann, G. Graw, R. Hertenberger, H. F. Wirth, and M. Jaskola, Phys. Rev. C **83**, 044614 (2011).

[31] G. Garcia-Bermudez, S. L. Gupta, N. C. Singhal, A. V. Ramayya, J. Lange, J. H. Hamilton, and N. R. Johnson, Phys. Rev. C **9**, 1060 (1974).

[32] Z. Gacsi and S. Raman, Phys. Rev. C **49**, 2792 (1994).

[33] J. L. Pore *et al.*, Eur. Phys. J. A **53**, 27 (2017).

[34] D. S. Cross *et al.*, Eur. Phys. J. A **53**, 216 (2017).

[35] J.-M. Régis and G. S. Simpson, *et al.*, Nucl. Instrum. Meth. Phys. Res. A **763**, 210 (2014).

[36] ENSDF, NNDC Online Data Service, ENSDF database, http://www.nndc.bnl.gov/ensdf/.

[37] M. Spieker, P. Petkov, E. Litvinova, C. Müller-Gatermann, S. G. Pickstone, S. Prill, P. Scholz, and A. Zilges, Phys. Rev. C **97**, 054319 (2018).

[38] J.-M. Régis *et al.*, Nucl. Instrum. Meth. Phys. Res. A **823**, 72 (2016).

[39] J.-M. Régis, M. Dannhoff, and J. Jolie, Nucl. Instrum. Meth. Phys. Res. A **897**, 38 (2018).

[40] J.-M. Régis et al. *et al.*, Nucl. Instrum. Methods Phys. Res., Sect. A **726**, 191 (2013).

[41] Z. Bay, Phys. Rev. **77**, 419 (1950).

[42] K. Löbner, in *The Electromagnetic Interaction in Nuclear Spectroscopy*, W.D. Hamilton (Ed.), North-Holland, New York, 1975, p. 173.

[43] J.-M. Régis *et al.*, Phys. Rev. C **95**, 054319 (2017).

[44] S. Ansari *et al.*, Phys. Rev. C **96**, 054323 (2017).

[45] A. Esmaylzadeh *et al.*, Phys. Rev. C **98**, 014313 (2018).

[46] R. Julin *et al.*, Nucl. Instrum. Methods **152**, 471 (1978).

[47] T. Otsuka and N. Yoshida, Program NPBOS, JAERI-M 85 report (Japan Atomic Energy Research Institute, 1985).

[48] G. Puddu, O. Scholten, and T. Otsuka, Nucl. Phys. A **348**, 109 (1980).

[49] K.-H. Kim, A. Gelberg, T. Mizusaki, T. Otsuka, and P. von Brentano, Nucl. Phys. A **604**, 163 (1996).

[50] P. D. Duval and B. R. Barrett, Phys. Lett. B **100**, 223 (1981).

[51] J. Jolie and K. Heyde, Phys. Rev. C **42**, 2034 (1990).

[52] M. Délèze, S. Drissi, J. Kern, P. Tercier, J. Vorlet, J. Rikovska, T. Otsuka, S. Judge, and A. Williams, Nucl. Phys. A **551**, 269 (1993).

[53] J. Jolie and H. Lehmann, Phys. Lett. B **342**, 1 (1995).

[54] H. Lehmann and J. Jolie, Nucl. Phys. A **588**, 623 (1995).